Thesis for The Degree of Licentiate of Engineering

Exploring the retrieval potential of the Ice Cloud Imager

Eleanor May

Department of Space, Earth and Environment
Chalmers University of Technology
Gothenburg, Sweden, 2024

Exploring the retrieval potential of the Ice Cloud Imager

Eleanor May

Department of Space, Earth and Environment
Division of Geoscience and Remote Sensing
Chalmers University of Technology
SE-412 96 Gothenburg,
Sweden
Phone: +46(0)31 772 1000

Cover:
Mountains of Clouds (Czar Hey, CC BY-SA 2.0,
https://www.flickr.com/photos/161174688@N08/51387194788)

Printed by Chalmers Digitaltryck,
Gothenburg, Sweden, 2024

Exploring the retrieval potential of the Ice Cloud Imager

Eleanor May

Department of Space, Earth and Environment
Chalmers University of Technology

Abstract

The upcoming Ice Cloud Imager (ICI) and the recently launched Arctic Weather Satellite (AWS) mark a new era in cloud ice observations. For the first time, continuous and global observations of the troposphere will be made at sub-millimetre wavelengths. Sub-millimetre observations are highly sensitive to larger ice crystals. These crystals contain a significant fraction of the ice mass in clouds which, despite their influence on Earth's climate, remain poorly understood. As a result, ICI and AWS will offer unparalleled data on atmospheric ice.

This thesis poses the question: What information on cloud ice can ICI observations provide? The primary objective of ICI is to provide ice cloud variables covering the entire atmospheric column. However, vertical information on ice has never before been derived from a passive microwave instrument. The question is therefore explored in two contexts: Firstly, how reliably will ICI fulfil its primary objective? Secondly, can we determine the vertical distribution of ice from ICI observations?

Since ICI is not yet launched, high-quality radiative transfer simulations of ICI are required to train the inversion model. Since there will be no co-locations of ICI with a radar providing cloud ice data, empirical retrievals will not be feasible after the launch. Consequently, the retrieval model used during ICI's operational phase must rely on the simulations. In this thesis, state-of-the-art simulations are presented, and a quantile regression neural network (QRNN) is used to produce probabilistic retrieval estimates.

The findings in this thesis indicate that ICI will produce reliable retrievals of the column-integrated variables: ice water path, mean mass height, and mean mass diameter, with a sensitivity to ice water paths ranging from $10\,\mathrm{g\,m^{-2}}$ to $10\,\mathrm{kg\,m^{-2}}$. The simulations pertaining to the column variables lay the foundation for the EUMETSAT level-2 ICI product. Vertical profiles of cloud ice are retrieved from ICI observations, achieving a resolution of $\sim$2.5 km.

Together, the observations from AWS and ICI will provide benefits to numerical weather prediction and deepen our understanding of ice clouds. The long-term cloud ice dataset from ICI will also support climate monitoring and validation of climate models. Furthermore, ICI could provide a truly novel dataset of vertical cloud ice, offering insights throughout the entire depth of an ice cloud.

Keywords Remote sensing, sub-millimetre, clouds, retrieval

Acknowledgments

I would like to express my deepest gratitude to my supervisor, Patrick Eriksson, for his guidance and support over these past years. His expertise and insights have been invaluable to this work, and in shaping my understanding of the field.

I am also grateful to all my colleagues at Chalmers. Our collaboration and insightful discussions have not only contributed to my research, but also brought genuine enjoyment to the process. I would also like to thank Simon Pfreundschuh for developing the exceptional QRNN Python package, which was truly indispensable to this work.

Finally, I thank Andreas for his constant support and encouragement. You and Elsa make sure I stay grounded through it all.

List of Works

Appended papers

This thesis is based on the following papers:

Paper 1. **E. May**, B. Rydberg, I. Kaur, V. Mattioli, H. Hallborn, and P. Eriksson. The Ice Cloud Imager: retrieval of frozen water column properties. *Atmos. Meas. Tech.* 17(19):5957-5987, 2024. doi: 10.5194/amt-17-5957-2024

Paper 2. **E. May**, and P. Eriksson. The Ice Cloud Imager: retrieval of frozen water mass profiles. *In preparation,* (2024).

Other works

Other relevant papers co-authored by Eleanor May:

J. Kukulies, A. Amell, H. Hallborn, **E. May**, P. Eriksson, and S. Pfreundschuh. The Chalmers Cloud Ice Climatology: A novel, robust climate record of frozen cloud hydrometeor concentrations. *J. Geophys. Res.* Submitted (2024).

Contents

List of Acronyms

ATBD	Algorithm Theoretical Basis Document
ATLID	Atmospheric Lidar
AWS	Arctic Weather Satellite
BMCI	Bayesian Monte Carlo Integration
CALIPSO	Cloud-Aerosol Lidar and Infrared Pathfinder Satellite Observations
CCIC	Chalmers Cloud Ice Climatology
CDF	Cumulative Distribution Function
CPR	Cloud Profiling Radar
GMI	Global Precipitation Measurement Microwave Imager
GPROF	Goddard Profiling Algorithm
ICI	Ice Cloud Imager
IPCC	Intergovernmental Panel on Climate Change
ISMAR	The International Submillimetre Airborne Radiometer
IWC	Ice Water Content
IWP	Ice Water Path
LEO	Low Earth Orbit
LWP	Liquid Water Path
MARSS	Microwave Airborne Radiometer Scanning System
MCMC	Markov Chain Monte Carlo
MODIS	Moderate Resolution Imaging Spectroradiometer
MWI	Microwave Imager
NWP	Numerical weather prediction
OEM	Optimal Estimation Method
PDF	Probability Density Function
PSD	Particle Size Distribution
QRNN	Quantile Regression Neural Network
WV	Water Vapour

Part I

Introductory chapters

1 Introduction

Atmospheric ice plays an important role in Earth's climate system, driving weather systems and strongly influencing Earth's energy budget. High-altitude ice clouds, such as cirrus and deep convective clouds, impact radiative forcing through the reflection of solar radiation and the modulation of outgoing long-wave radiation (Matus and L'Ecuyer, 2017). The radiative properties of ice clouds depend on several factors, including cloud height and the mass of ice contained within the cloud. If liquid water coexists with ice in a cloud, the net effect on radiation is further impacted. Overall, ice clouds lead to a net warming of the Earth (Matus and L'Ecuyer, 2017).

In addition to its radiative impact, atmospheric ice also plays an important role in the hydrological cycle through its influence on atmospheric processes. The formation of ice releases latent heat, which drives atmospheric circulation. In deep convective systems, this release of heat determines the formation and the dynamics of storms (Bony et al., 2015). Ice clouds are also central to precipitation. Through the growth and melting of cloud ice crystals, water is redistributed through the atmosphere and ultimately reaches the surface. In fact, over land outside the tropics, ice clouds are involved in 99% of rainfall events (Mülmenstädt et al., 2015). Although the atmosphere constitutes the smallest reservoir of water within the Earth system, large amounts of energy, in the form of moisture and heat, are rapidly exchanged between Earth's atmosphere and surface.

Knowledge of atmospheric ice is undoubtably essential for accurate weather prediction, management of water resources, and understanding Earth's climate. As a result, cloud ice has been recognised as an essential climate variable (Space - WGClimate, 2024). However, despite its importance, our knowledge remains incomplete. A deeper understanding of the formation and microphysics of ice clouds is needed. Additionally, we are yet to know how the distribution and frequency of ice clouds might change in response to a warming of the planet. Such changes in ice clouds are likely to trigger further shifts in weather patterns and the wider climate system. However, the extent of this impact remains unclear; there are still gaps regarding the exact role of atmospheric ice in the water cycle and the Earth's radiation budget. According to the Intergovernmental Panel on Climate Change (IPCC), clouds are the largest source of uncertainty in climate feedbacks (IPCC, 2021). Therefore, in light of

the current changing climate, improving our understanding of ice clouds is an urgent issue.

The need for improved understanding is evident in the fact that climate models have long struggled to represent clouds accurately (IPCC, 2021; Stephens, 2005; Waliser et al., 2009). The ability to evaluate and constrain climate models under a variety of weather and climate conditions improves if long-term global cloud ice datasets are used. Such datasets also act as a useful benchmark for comparisons between climate models.

However, datasets of common cloud ice variables, such as ice water path (IWP), are limited in number and do not show good agreement (Duncan and Eriksson, 2018). The disagreement arises partially due to varying sensitivity to cloud properties; many of the currently operational sensors are unable to detect all ice particles, either due to the particle size or the particle's depth within a cloud. Other contributing factors include differing spatial and temporal coverage between satellites, and the need for model assumptions when retrieving cloud ice information from satellite observations. Finally, even the definition of atmospheric ice variables can vary. For example, it is often unclear whether a dataset includes frozen precipitation within a column of atmospheric ice.

We can improve our understanding of atmospheric ice by making progress in three important areas. Firstly, we need sensors that are specifically sensitive to cloud ice. This includes sensitivity throughout the entire cloud column, and across the range of ice crystal sizes. Only a sensor with high sensitivity to ice can accurately capture variations in ice properties across a variety of atmospheric conditions. Secondly, it is essential that we have a strong understanding of the physical processes behind the observations. This is non-trivial, due to factors such as the complexity of scattering from ice crystals. A strong understanding of the physics can provide insight into how satellite retrievals behave, and how any underlying physical assumptions might influence them. Finally, we need retrieval methods that produce results that are not only accurate, but also realistically reflect the inherent uncertainties associated with the problem. By addressing these challenges, we can develop reliable cloud ice datasets. In turn, these datasets can support climate models and deepen our understanding of the behaviour and impact of atmospheric ice.

2 Remote sensing of atmospheric ice

2.1 Introduction to satellite remote sensing

Remote sensing is the process of acquiring information on the characteristics of a target from a distance. In the context of satellites, the information is determined using sensors aboard a satellite that measure the interaction and propagation of electromagnetic radiation.

The use of satellites allows for observations of large areas of Earth, including inaccessible regions. Observations of a specific area can be repeated regularly, leading to consistent and long-term measurements. Satellite remote sensing of the Earth can be employed for many uses, including gathering information on the atmosphere, the Earth's surface, oceans, and vegetation. However, it is important to note that a remote sensing measurement is an indirect measurement. In other words, remote sensing techniques provide one or more measurements of electromagnetic radiation, from which an estimate of a geophysical quantity can be retrieved.

Alternatives to satellite remote sensing include airborne remote sensing and in-situ methods. In-situ measurements can be useful since they provide highly detailed information in a localised area. For example, direct in-cloud measurements can provide information on small-scale cloud features, such as cloud particle size and shape, but are constrained to a specific location. In contrast, airborne missions have the benefit of flexibility. Specific areas of interest can be observed more frequently, since the missions are not limited to pre-determined orbits as satellites are. However, satellites are indispensable for providing a consistent and global view, and understanding large-scale dynamics.

Satellites can be categorised in various ways. Often, they are grouped according to their orbit type. Geostationary satellites have an orbit period identical to Earth's orbit, and thus are stationary relative to a specific location on Earth. This allows for very frequent measurements over the observed area. Achieving this orbital period requires the satellite to be placed over the equator at an altitude of $\sim$36 000 km. As a benefit of their high altitude, the observed

area can cover a third of the Earth's surface. However, the spatial resolution of a geostationary satellite is a limiting factor. The minimum angular separation of a satellite can be estimated according to the Rayleigh criterion:

$$\theta = 1.22\frac{\lambda}{D} = \frac{x}{d}. \tag{2.1}$$

In the above relation, λ is wavelength, D is the diameter of the satellite antenna, d is the distance of the satellite from Earth, and x is the satellite on-ground spatial resolution. It is evident that, due to the high altitude of geostationary satellites and practical limits on antenna size, the spatial resolution at microwave wavelengths becomes too low to be useful. Therefore, only visible and infrared sensors are used on geostationary satellites.

Satellites with a low Earth orbit (LEO) are located at much lower altitudes than geostationary satellites, ranging between 500 km and 850 km. They orbit the Earth more frequently as a result, but each observation covers a much smaller area compared to that of a geostationary satellite. The orbits of LEO satellites can be further divided into two categories: polar orbits and low inclination orbits. Polar orbiting satellites pass close to the poles in each orbit. Their orbits are often also sun-synchronous. In a sun-synchronous orbit, a given area is measured at the same times every day, producing a consistent view of the target. Satellites with low inclination orbits observe at a lower angle relative to the Earth's equator than polar-orbiting satellites do. As such, they are not sun-synchronous, which provides the benefit of producing information on the diurnal cycle at a given location.

Satellites can also be grouped according to whether they are active or passive sensors. Active sensors emit electromagnetic signals and measure how the signal is reflected from the target back to the sensor. Passive sensors do not emit a signal. Instead, they measure emitted and reflected radiation originating either from the Earth's surface, the atmosphere, or the Sun.

Another, and perhaps the most important, way of categorising satellites is the frequency of radiation measured. A satellite measures either reflected radiation sent from the satellite itself, reflected solar radiation, or emitted radiation. This radiation is measured at one or multiple specific frequencies. All objects with a temperature more than 0 K will emit radiation. The amount of emission, and the frequency of the emitted radiation, is proportional to the emissivity and the temperature of the object. Scattering is also a consideration. Radiation may be scattered by objects it encounters, and the amount of scattering will depend on the frequency of the incoming radiation and the properties of the object. Finally, some radiation may be absorbed by a material it encounters, and the amount of absorption will be dependent on the frequency.

However, simply choosing a frequency such that we are sensitive to a particular target is not necessarily straightforward. The measured signal must propagate through the atmosphere to reach the satellite sensor. Clouds, gases

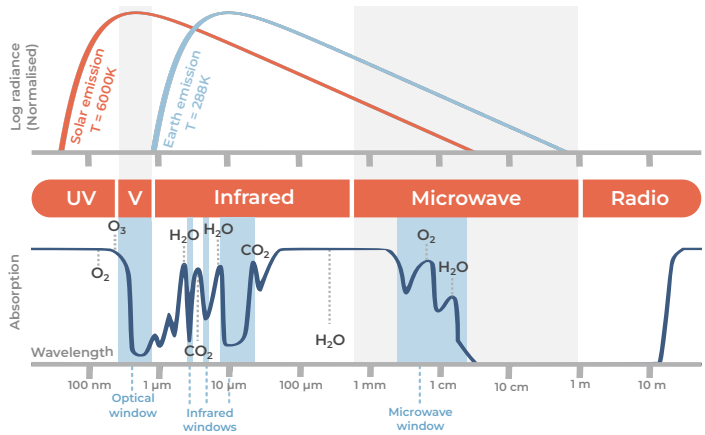

Figure 2.1: Illustration of the atmospheric absorptivity in the zenith direction (bottom), ranging from UV to radio wavelengths, accompanied by the species contributing most to the absorption at a given wavelength. Atmospheric windows are indicated in blue. In reality, the microwave window extends to longer wavelengths, evident in the very low absorption occuring up to wavelengths of more than 10 m. However, the range of the microwave window shown is chosen to correspond to observations of atmospheric water, with the upper limit associated with precipitation radars. The normalised spectral radiance $B_\lambda(T)$ of two blackbodies (see Section 3.1) is also shown (top). Solar emission peaks in the visible (V) region of the spectrum. Earth's emission peaks in the infrared region, but remains relatively strong at microwave wavelengths, motivating measurements by passive microwave sensors.

and aerosols are not equally distributed in the atmosphere, and the strength of the processes of scattering, absorption and emission will vary with altitude. At some frequencies, one of these processes may be particularly strong, and the signal will be dominated by the process at that altitude. This leads to a sensitivity to different levels of the atmosphere that is dependent on frequency.

Observations therefore exploit different parts of the electromagnetic spectrum in order to gather the desired information. For high sensitivity to an object that emits radiation, passive sensors consider frequencies at which relatively high emission occurs. In the case of active sensors, strong backscatter is desired. Additionally, areas of the spectrum are avoided to reduce loss of the signal due to absorption. For example, observations of the Earth's surface will not be made at frequencies which are associated with strong atmospheric absorption, since the information on the surface will be lost. Surface measurements instead make use of specific regions of the electromagnetic spectrum with lower absorption. These are known as atmospheric windows, and are illustrated in Fig. 2.1. Examples of these windows include the optical window located between 300 nm and 2 µm and the infrared window between 8 µm and 14 µm.

2.2 Instrument sensitivity to ice cloud properties

The remote sensing of ice clouds derives information from the fact that atmospheric ice absorbs, emits, and scatters radiation at various atmospheric levels. Therefore, to obtain information on an ice cloud, we desire a signal that interacts strongly with ice cloud particles, preferably throughout the entire column of cloud, while minimising atmospheric attenuation.

Active sensors, such as radar and lidar, are able to provide information on an entire column of cloud. Lidar is particularly sensitive to small liquid cloud droplets due to its high frequency (Cesana et al., 2023). However, a lidar signal can be quickly attenuated by thick clouds. On the other hand, radar is highly suited to measure cloud ice and precipitation. Its lower frequency compared to lidar translates to higher sensitivity to larger particles. This includes precipitating hydrometeors and cloud ice, albeit primarily larger ice crystals. When used together, lidar and radar measurements are powerful; they can provide detailed information on the vertical structure of both frozen and liquid atmospheric water. However, these sensors have several limitations. Firstly, due to a very narrow swath width, the observations have essentially two-dimensions: along-track and vertical. As a result, many orbits are required to achieve global coverage. Secondly, radars typically measure at one single frequency. This corresponds to only one degree of freedom in the observation. Since the geophysical quantity of interest is only an estimate of a quantity derived from an observation, further assumptions are generally required to improve or constrain the estimate. In turn, this can lead to high uncertainties in the estimated variable.

In the realm of passive sensors, optical, infrared, and microwave frequencies are often used to observe atmospheric ice. However, this group of sensors span a wide range of frequencies. Sensitivity to various cloud properties can therefore vary significantly.

Optical sensors measuring in the visible part of the electromagnetic spectrum detect reflected sunlight. The sensitivity of these sensors is comparable to the human eye. Due to the atmospheric window in the visible region, the atmosphere appears transparent to our eyes. However, clouds are generally visible. When visible, they appear nearly or completely opaque, and a often a bright white colour. This effect arises from strong scattering of sunlight towards our eyes or, in the case of satellite observations, back towards the sensor. Since there is such a high contrast between the background atmosphere and the cloud, optical sensors can provide detailed information on horizontal cloud structure. However, visible observations have two main limitations: they cannot observe clouds during the night, and they contain very limited information from below the cloud top due to strong scattering.

Since clouds emit thermal infrared radiation, infrared frequencies are effectively used to observe ice clouds. However, ice clouds are also relatively opaque at infrared frequencies. Most radiation emitted from the lower layers of a cloud is absorbed or scattered before it is able to pass up through the cloud and reach the sensor. As a result, infrared sensors are primarily sensitive to the cloud top. While infrared sensors can effectively detect the presence of an ice cloud and be used to retrieve useful information such as cloud top height, their measurements generally contain limited information on the full cloud column. However, there do exist successful retrievals of vertical information from infrared measurements, which is discussed further in Section 2.3.

Decreasing in frequency from infrared to microwave, the signal is able to penetrate further into the cloud. However, nearly all currently operational passive microwave sensors measure at frequencies 183 GHz and below. This is equivalent to wavelengths of ∼1.5 mm and larger, which are similar in size to large liquid water cloud droplets or precipitation. Therefore, although most existing passive microwave sensors are highly sensitive to liquid water, they are less suited to the detection of smaller ice crystals.

However, there exists a gap in observations. Between the highest frequency of most current microwave observations and the lowest frequency of infrared observations lies the sub-millimetre region. This region covers frequencies greater than ∼300 GHz, which corresponds to wavelengths smaller than 1 mm. Observing at these wavelengths increases sensitivity to ice crystals. Despite the suitability of sub-millimetre sensors for ice cloud measurements, there are a limited amount of sub-millimetre observations available. However, a new wave of passive microwave and sub-millimetre sensors are paving the way for better observations of atmospheric ice.

2.3 Current atmospheric ice mass observations

Many satellite missions have been designed and launched with the aim to observe ice clouds. These missions provide us with valuable information, including cloud location, altitude, temperature, thermodynamic phase, structure, and mass. Knowledge of the mass of ice contained within a cloud is useful due to its connection to the radiative forcing of ice clouds and to the production of both frozen and liquid precipitation. The mass of ice can be characterised using the variable ice water content (IWC), in $\mathrm{kg\,m^{-3}}$. Alternatively, the total mass of ice within an atmospheric column is characterised by IWP, in $\mathrm{kg\,m^{-2}}$. This section presents a brief summary of some of the key sensors measuring ice mass, although the list is not exhaustive. The currently operational and future planned satellite-based sensors discussed in this section are also shown in Fig. 2.2, alongside the region of the electromagnetic spectrum that they observe in.

Currently, the most reliable global source of ice mass data originates from the CloudSat 94 GHz radar and the Cloud-Aerosol Lidar and Infrared Pathfinder

Satellite Observation (CALIPSO). DARDAR (Delanoë and Hogan, 2010) and 2C-ICE (Deng et al., 2010) are two of the most widely used datasets containing CloudSat- and CALIPSO-based retrievals of cloud ice properties. Since the launch of CloudSat and CALIPSO in 2006, DARDAR and 2C-ICE have provided unparalleled datasets of IWC. However, as discussed in Section 2.2, retrievals based on a single radar observation must incorporate multiple microphysical assumptions. Such assumptions translate into relatively high uncertainties for retrieved IWC in DARDAR (Heymsfield et al., 2008). Both CloudSat and CALIPSO ceased operations in 2023.

In May 2024, ESA's Earth Cloud Aerosol and Radiation Explorer (EarthCARE) (Illingworth et al., 2015) was launched. Included on board the satellite is the Atmospheric Lidar (ATLID), measuring at 355 nm, and the Cloud Profiling Radar (CPR), measuring at 94 GHz. Together, the radar and lidar will provide high-resolution information on the vertical structure of both liquid and ice clouds. The reliable IWC data available with EarthCare observations provides essential continuity after the decommissioning of CloudSat and CALIPSO.

There exist multiple passive sensors, measuring at infrared and visible wavelengths, that offer data on cloud ice. One of which is the Moderate Resolution Imaging Spectroradiometer (MODIS), hosted on the sun-synchronous Aqua and Terra satellites as part of NASA's Earth Observing System (EOS). MODIS measures at both visible and infrared wavelengths (Platnick et al., 2003). As discussed in Section 2.2, retrievals of IWP from such observations are generally cloud-top estimates. However, there are recent efforts to develop retrieval schemes that make use of geostationary infrared observations to retrieve cloud ice profiles. The Chalmers Cloud Ice Climatology (CCIC, Amell et al., 2024) is a dataset that retrieves IWC, IWP, cloud masks, and cloud classification from a single infrared observation. This is made possible by training a neural network to make use of spatial information contained in geostationary imagery, using 2C-ICE as target data.

Moving into the microwave region of the electromagnetic spectrum, there are several existing passive microwave observations that provide ice mass information. For example, IWP estimates are offered by the Goddard Profiling Algorithm (GPROF, Kummerow et al., 2015), a retrieval scheme based on the Global Precipitation Measurement Microwave Imager (GMI). However, the relatively low frequencies of the GMI channels (10 GHz to 183 GHz) correspond to low sensitivity to ice hydrometeors. This means that precipitation is its primary focus, with IWP provided as a secondary output.

The first strides forward into sub-millimetre observations of ice clouds were made by three limb sounding instruments. Although their objective was to monitor atmospheric gases, retrievals of ice mass were successfully performed for Aura MLS (Wu et al., 2006), Odin/SMR (Eriksson et al., 2007), and SMILES (Eriksson et al., 2014; Millán et al., 2013).

Several flight campaigns also exist that measure at sub-millimetre wavelengths. The International Submillimetre Airborne Radiometer (ISMAR) is an airborne instrument designed to act as a demonstrator for the upcoming Ice Cloud Imager (ICI) instrument, measuring at frequencies between 118 and 664 GHz. Brath et al. (2018) combined microwave and flight campaign observations, including ISMAR, and demonstrated that significant improvement in the retrievals occurs with the inclusion of the sub-millimetre observations. A similar conclusion was drawn by Pfreundschuh et al. (2022) when combining radar measurements with sub-millimetre flight campaign data.

However, it was not until 2024 that the first operational sub-millimetre mission was launched — the Arctic Weather Satellite (AWS, eoPortal, 2024). AWS measures at frequencies between 50.3 GHz to 325.15 GHz. The lower frequency channels ($<$89 GHz) support temperature sounding. Higher frequency channels ($\geq$89 GHz) are used for humidity sounding and cloud detection. Unlike the limb sounding missions, AWS is specifically designed to provide cloud observations. These observations, and in particular the novelty of the sub-millimetre channels, establish AWS as a mission of high scientific value. AWS was developed by the European Organisation for the Exploitation of Meteorological Satellites (EUMETSAT) as a prototype satellite for a full constellation of satellites: EUMETSAT Polar System – Sterna (EPS-Sterna, EUMETSAT, 2024). Pending final approval in 2025, the first of the EPS-Sterna satellites is expected to be launched in 2029. Together, the satellites will observe over 90% of Earth in approximately 5 hours, offering an unparalleled worldwide dataset of sub-millimetre observations.

Although AWS measures at a maximum of 325 GHz, this is not the upper limit for frequencies suited to measure cloud ice. Both the aforementioned limb sounding retrievals and the flight campaign-supplemented retrievals demonstrate that even higher frequency channels can benefit the retrieval of ice mass. A channel at a frequency of 664 GHz is in fact highly suited to the measurement of smaller ice crystals due to the comparable size of the wavelength and the particle radius.

Despite the fact that there are currently no operational sensors with frequencies greater than 325 GHz, the future is promising. With the launch of ICI will arrive observations within a frequency range of 183 GHz to 664 GHz. Further details on ICI are given in Chapter 5. While the objective of AWS is to support numerical weather prediction (NWP), officially offering only radiances, ICI is designed specifically for the retrieval of column ice mass variables. The launch of ICI will therefore provide a completely novel dataset on cloud ice, which will be highly valuable to our understanding of atmospheric ice.

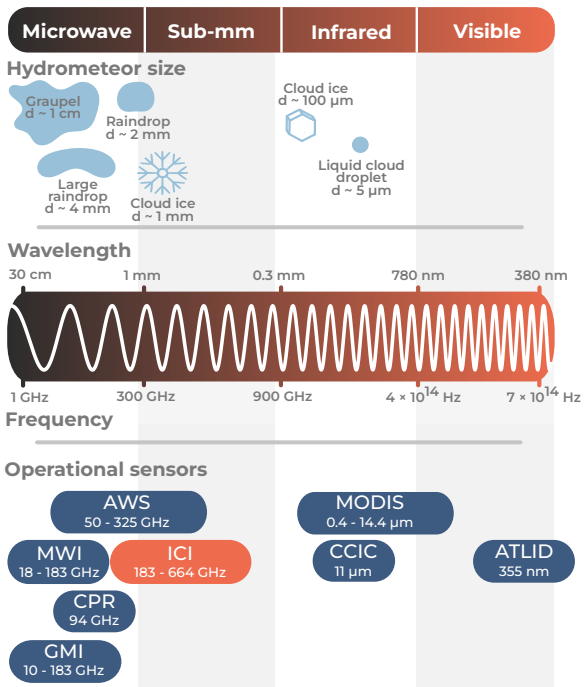

Figure 2.2: An illustration of the range of the electromagnetic spectrum used to observe clouds and precipitation, and several of the current operational sensors measuring within this range. Also shown are examples of various-sized hydrometeors present in the atmosphere. When radiation wavelength is comparable to particle size, the sensor is particularly sensitive to the presence of such particles. Note that rain droplets fall within the range of the spectrum measured by the Microwave Imager (MWI). This is due to their large diameter, although the large droplets shown here are relatively rare. In contrast, ICI covers a wavelength range more suited to the measurement of ice crystals.

3 Microwave radiative transfer

3.1 Emission

The process of emission is fundamental to understanding and interpreting passive microwave remote sensing observations. Emission refers to the process by which a body radiates energy in the form of electromagnetic radiation. All bodies with a temperature greater than 0 K will emit electromagnetic radiation. Measurement of this radiation by microwave satellite sensors can provide information on the object's physical properties.

Emission by a molecule occurs at discrete frequencies, corresponding to a molecular transition defined as a change in a molecule's energy state. Such transitions can be vibrational, rotational, or electronic, where the type of transition is associated to a certain frequency range. The emission at a specific frequency is represented as a spectral line along the electromagnetic spectrum. For a solid consisting of many molecules, such a large number of spectral lines are present that the emission spectrum appears effectively continuous across a range of frequencies.

When discussing emission, it is helpful to introduce the concept of a blackbody. A blackbody is defined as an idealised object which absorbs all incident radiation. A blackbody in thermal equilibrium emits radiation. The intensity of the radiation emitted by a blackbody is isotropic, and given by Planck's law:

$$B_\lambda(T) = \frac{2hc^2}{\lambda^5}\left(\frac{1}{e^{hc/\lambda kT} - 1}\right). \tag{3.1}$$

I_λ is the intensity at wavelength λ, h is Planck's constant, k is Boltzmann's constant, c is the speed of light, and T is the temperature of the blackbody. The spectrum of $B_\lambda(T)$ as a function of wavelength peaks at a specific wavelength depending on temperature. At higher temperatures, $B_\lambda(T)$ tends towards shorter wavelengths. Using Eq. 3.1, the temperature of a blackbody body can be determined by observing the emission at a single wavelength.

Integrating the Planck function over all wavelengths provides the irradiance F of an object, defined as the rate at which energy is transferred through a

unit area. This is known as the Stefan-Boltzmann law, and is written as

$$F = \sigma T^4, \tag{3.2}$$

where F has the unit W m^{-2} and σ is the Stefan-Boltzmann constant. If the irradiance from the blackbody is known, its temperature can be calculated.

In reality, most objects are not perfect emitters like blackbodies. To characterise the intensity of the radiation an object emits relative to that of a blackbody at the same temperature, we introduce the emissivity ϵ_λ, where $\epsilon_\lambda \in [0, 1]$. The emissivity acts on the blackbody intensity to give the spectral radiance I_λ of the object:

$$I_\lambda = \epsilon_\lambda B_\lambda. \tag{3.3}$$

The emissivity of an object is dependent on its physical properties, including surface roughness or moisture content. The emissivity also varies according to the properties of the electromagnetic radiation being observed, such as the frequency, the incidence angle, and the polarisation state.

If the object in question is not a blackbody, i.e. not a perfect emitter, then the inverse of Eq. 3.1 can be used to find the equivalent blackbody temperature. In other words, it finds the temperature of a blackbody that would emit the equivalent amount of measured radiance to the non-blackbody. In the context of microwave remote sensing, this is referred to as the *brightness temperature* T_b.

3.2 Characterising radiation

Electromagnetic waves carry energy that can be separated into the contributions from individual wavelengths. The rate of energy E transferred in a given direction per unit area and unit time and at a specific wavelength λ is expressed through the monochromatic intensity I_λ as

$$I_\lambda = \frac{dE}{d\Omega d\lambda}, \tag{3.4}$$

where Ω is the solid angle. The energy emitted by an object generally spans a broad range of wavelengths. Integrating I_λ over some range of the electromagnetic spectrum, such as the band of frequencies observed by a sensor, gives us the intensity, or radiance, I:

$$I = \int_{\lambda_1}^{\lambda_2} I_\lambda d\lambda. \tag{3.5}$$

The radiance has units W m^{-2} sr^{-1}.

The irradiance F is obtained by integrating I over the hemisphere of solid angle extending over the incident place and the wavelength:

$$F = \int_{\lambda_1}^{\lambda_2} \int_{2\pi} \cos\theta I_\lambda d\omega d\lambda. \tag{3.6}$$

θ is the angle between the incident radiation and the normal to the plane.

3.3 Radiative transfer in clear-sky conditions

In order to understand how emitted radiation is measured by a sensor, it is important to consider how radiation behaves as it propagates through the atmosphere. During propagation, the radiation interacts with atmospheric components and undergoes changes in energy. The amount of energy transferred is affected by absorption, emission, and scattering.

To characterise the amount of transmission through the atmosphere in both clear-sky and cloudy conditions, the optical depth τ can be used. The transmissivity t of a layer of atmosphere is defined as

$$t_\lambda = e^{-\tau_\lambda \sec\theta}, \tag{3.7}$$

where θ is the zenith angle. τ can be described as a measure of how the intensity of the radiation would be reduced due to absorption and scattering if it passes through an atmospheric layer at zenith. Within the microwave region of the electromagnetic spectrum, the radiation wavelength is long relative to the size of molecules and aerosols in the air. Therefore, in clear-sky conditions, scattering effects may be neglected. In this case, τ is governed by the presence of atmospheric gases and the wavelength of the radiation considered.

Atmospheric gas molecules will absorb incoming radiation. How effective a single particle, such as a molecule of gas, is at absorbing radiation can be defined through its absorption cross-section σ_a. This can be thought of as an effective area over which the particle absorbs radiation. A monochromatic beam's reduction in energy due to absorption by a number of particles per unit volume N is then given by

$$\frac{dI_\lambda}{ds} = -I_\lambda N \sigma_a. \tag{3.8}$$

However, σ_a is a quantity that describes a microscopic property. When considering a large quantity of molecules within the atmosphere, it is more useful to use a macroscopic quantity, and therefore we introduce the absorption coefficient κ_a as

$$\kappa_a = N\sigma_a, \tag{3.9}$$

where N is the number of particles per unit volume. The solution to Eq. 3.8 then becomes

$$I_\lambda = -I_{\lambda,0} e^{-\int_0^s \kappa_a(s')ds'}, \tag{3.10}$$

where κ_a is dependent on distance $s^{'}$ due to the concentrations of gases varying within the propagation path of the beam from 0 to s. The total fraction of radiation $I_\lambda / I_{\lambda,0}$ that is absorbed can be characterised by the absorptivity a_λ, giving

$$I_\lambda = a_\lambda I_{\lambda,0}. \tag{3.11}$$

In the absence of scattering, a_λ can be related to the transmissivity t_λ by

$$a_\lambda = 1 - t_\lambda, \tag{3.12}$$

and the optical depth τ is given by

$$\tau = \int_0^s \kappa_a(s^{'}) ds^{'}. \tag{3.13}$$

In this context, τ represents the total amount of absorption occurring along the path of the beam.

To relate absorptivity and emissivity, we can apply Kirchoff's law, defined as

$$\varepsilon_\lambda = a_\lambda. \tag{3.14}$$

Kirchoff's law is not applicable over the entirety of the atmosphere. The law requires the assumption of equilibrium, but the atmosphere is not isotropic and the temperature is not uniform throughout. However, if one assumes a constant temperature and mean gas concentrations within small localised volumes of the atmosphere, local thermodynamic equilibrium can be assumed. For microwave radiation, this is applicable in the atmosphere at altitudes below ∼100 km.

For microwave radiation propagating through cloud-free sky, the intensity reaching a point s_1 is the total emission in the given direction, minus loss due to absorption. Since emission and absorption are equal under the above assumptions, the rate of change of intensity with respect to distance is given by

$$\frac{dI_\lambda}{ds} = -\kappa_{a,\lambda} I_\lambda + \kappa_{a,\lambda} B_\lambda(T). \tag{3.15}$$

This is known as *Schwarzchild's equation*. Integrating Schwarzchild's equation along the path of propagation results in

$$I_\lambda(s) = \underbrace{I_{\lambda,0} e^{-\tau_\lambda(s,0)}}_{\text{Attenuation}} + \underbrace{\int_0^s B_\lambda(T_{s_i}) e^{-\tau_\lambda(s,s_i)} ds_i}_{\text{Emission}}. \tag{3.16}$$

The first term of the above equation represents the intensity of the radiation at point $s_i = 0$ decreasing due to absorption, and finally reaching point s. The second term represents a sum over thin atmospheric layers that the radiation passes through. Each ith layer has a temperature $T(s_i)$ and thus emits radiation. The radiation emitted by each layer is also attenuated as it travels from

s_i to s, represented by the factor $e^{-\tau_\lambda(s,s_i)}$ in the second term.

Schwarzchild's equation is a general case and can be applied to both upward and downward looking radiometers. In the context of a downward looking satellite, the first term in Schwarzchild's equation represents radiance from the surface and the second term represents emission from atmospheric layers, the received signal contains information on both the surface and the atmosphere. Furthermore, since the first term also accounts for absorption in the atmosphere, information in the form of gas concentrations is also contained in this term. The second term contains additional information on the atmospheric layers, such as layer temperatures. The strength of the signal from either surface or atmospheric layer depends on the sensitivity of radiation to the surface or given atmospheric layer at the chosen wavelength.

3.4 Radiative transfer in the presence of ice

In the presence of larger particles in the atmosphere, such as cloud particles or precipitation, the scattering of microwave radiation must also be considered. When a beam of radiation passes through a cloud, the radiation will undergo a degree of extinction dependent on the concentration of cloud particles and their effectiveness as scatterers.

The intensity of an electromagnetic wave incident on a single particle will decrease, as some incident power is absorbed by the particle and some is scattered. The effectiveness of a particle to absorb or scatter radiation can be defined in terms of the extinction cross-section σ_e, which is a sum of the scattering cross-section σ_e and the absorption cross-section σ_e:

$$\sigma_e = \sigma_a + \sigma_s. \tag{3.17}$$

The extinction characteristics of a single cloud particle are dependent on wavelength, refractive index/dielectric constant, and particle radius.

When considering a volume of ice particles, we define the extinction coefficient κ_e as

$$\kappa_e = \kappa_a + \kappa_s. \tag{3.18}$$

κ_e can be interpreted as a measure of how effective the particles within a volume are at decreasing the intensity of incident radiation through absorption and scattering. The decrease in the intensity of radiation passing through the volume is analogous to Eq. 3.8, and will therefore decrease according to

$$\frac{dI_\lambda}{ds} = -I_\lambda(\lambda)N\sigma_e = -I_\lambda\kappa_e(\lambda). \tag{3.19}$$

Another important parameter used to characterise the particles is the single scattering albedo $\omega(\lambda)$, defined as

$$\omega(\lambda) = \frac{\kappa_s}{\kappa_s + \kappa_a}. \tag{3.20}$$

The above relation summarises the importance of scattering relative to absorption. Additionally, the asymmetry parameter is useful when describing scattering. It is defined as

$$g(\lambda) = \frac{1}{2} \int_{-1}^{1} P(\cos\theta^{'}) \cos\theta^{'} \, d\cos\theta^{'}, \tag{3.21}$$

where $g(\lambda) \in [-1, 1]$. $\theta^{'}$ is the angle between the incident radiation and the scattered radiation. $P(\cos\theta^{'})$ is the scattering phase function. If the scattered radiation is isotropic, then $g(\lambda) = 0$. Positive values of $g(\lambda)$ imply that forward scattering is dominant. For cloud ice particles, $g(\lambda) \sim 0.8$.

Both absorption and scattering are governed by the particle's complex dielectric constant $\varepsilon = \varepsilon^{'} + \varepsilon^{''}$. For ice, the relative permittivity $\varepsilon^{'}$ in the microwave region (10 MHz to 300 GHz) is small relative to that of water. $\varepsilon^{'}$ is also close to independent of frequency. The dielectric loss factor $\varepsilon^{''}$ is much smaller than the permittivity $\varepsilon^{'}$ but displays both a frequency and temperature dependence. The absorption coefficient can be approximated by

$$\kappa_a \propto \frac{\varepsilon^{''}}{\sqrt{\varepsilon^{'}}}. \tag{3.22}$$

Therefore, for the microwave range of the spectrum, ice particles are weak absorbers of radiation. Therefore, the impact of absorption from ice particles can be largely neglected at microwave frequencies.

The simplest approach to modelling scattering is to assume that the radiation is scattered by a spherical particle with radius r. One can then assign a size parameter x, defined as

$$x = \frac{2\pi r}{\lambda}. \tag{3.23}$$

If the particle has a size parameter $x \ll 1$, it is a relatively inefficient scatterer, and we are within the Rayleigh scattering regime. For larger x ($x \geq 0.1$), we are in the Mie scattering regime. Most ice crystals are small enough to be in the Rayleigh regime for microwave radiation. However, there do exist larger ice crystals which fall within the Mie regime for microwave radiation, and these larger particles dominate the impact on observed T_{b}. In the case of these larger crystals, scattering calculations become more complicated. Analytical expressions for Mie scattering exist for homogeneous spheres of ice, but are not applicable to actual ice crystals, which are typically non-spherical. Instead, numerical methods are required to model scattering.

The intensity of scattered, absorbed, or emitted radiation also depends on the polarisation state of the incoming wave. To characterise the dependency of intensity on polarisation, it is useful to define the Stokes vector $\mathbf{I}$ whose four

elements describe the polarisation state of an electromagnetic wave:

$$\mathbf{I} = \begin{bmatrix} S_0 \\ S_1 \\ S_2 \\ S_3 \end{bmatrix} = \begin{bmatrix} \langle E_{0x}^2 \rangle + \langle E_{0y}^2 \rangle \\ \langle E_{0x}^2 \rangle - \langle E_{0y}^2 \rangle \\ \langle 2E_{0x}E_{0y}\cos(\phi_y - \phi_x) \rangle \\ \langle 2E_{0x}E_{0y}\sin(\phi_y - \phi_x) \rangle \end{bmatrix} \tag{3.24}$$

The brackets $\langle\rangle$ are time averages and $(\phi_y - \phi_x)$ is the phase difference between the x and y components of the wave.

In reality, when an electromagnetic wave is scattered, its direction, intensity, and polarisation may change. These changes are captured in the (4×4) scattering matrix $\mathbf{Z}$, which modifies the Stokes vector of the incident wave. The Stokes vector of the scattered wave is related to the incident wave by

$$\begin{bmatrix} S_0^s \\ S_1^s \\ S_2^s \\ S_3^s \end{bmatrix} = \frac{1}{R^2}\mathbf{Z} \begin{bmatrix} S_0^i \\ S_1^i \\ S_2^i \\ S_3^i \end{bmatrix}. \tag{3.25}$$

The next step is to derive the full equation to describe the change in intensity along a path s due to absorption, scattering, and emission. Firstly, we move to a three-dimensional vector formalisation, where $\mathbf{r}$ is the position and $\mathbf{n}$ is the direction of propagation. The absorption coefficient is instead represented by the absorption vector $\boldsymbol{\alpha}$. Combining Schwarzchild's equation with the consideration of scattering, we can define *the radiative transfer equation* as

$$\frac{d\mathbf{I}(\lambda, \mathbf{r}, \mathbf{n})}{ds} = -\mathbf{K}\mathbf{I}(\lambda, \mathbf{r}, \mathbf{n}) + \boldsymbol{\alpha}\mathbf{B}(\lambda, \mathbf{r}, \mathbf{n}) + \int_{4\pi} \mathbf{Z}(\lambda, \mathbf{r}, \mathbf{n}, \mathbf{n}')\mathbf{I}(\lambda, \mathbf{r}, \mathbf{n}')d\mathbf{n}', \tag{3.26}$$

where $\mathbf{n}'$ is the propagation direction towards $\mathbf{n}$. $\mathbf{K}$ is the extinction matrix, which is the sum of the absorption vector and the radiation scattered out of the direction of propagation. The integral term on the far right represents the scattering of radiation into the direction of propagation.

3.5 The characterisation of ice clouds

Now that the characteristics of ice particles within a cloud have been defined, it is also useful to introduce several parameters that characterise the ice clouds themselves: the particle size distribution, the water content per unit volume, and the mean volume-weighted diameter.

Ice particles within a cloud vary in size and shape. So far, we have assumed a spherical particle with radius r. However, characterising the size of an ice crystal is not as straightforward as assumed in this chapter, primarily because ice crystals do not have a simple shape. To represent the size, a form of parameterisation is needed. One example is the use of the volume equivalent

diameter D_{veq}, defined as the diameter of a sphere of ice with the same mass as the crystal under consideration. D_{veq} is defined as

$$D_{veq} = \left(\frac{6m}{\pi\rho}\right)^{\frac{1}{3}}, \tag{3.27}$$

where m is the mass of the ice particle, and ρ is the density of ice. There exist alternative ways to represent the size of ice particles. Therefore, it is important to note that although the remainder of the expressions given in this section are formulated using D_{veq}, the same expressions may be defined differently with another size parameterisation.

The particle size distribution $p(D)$, or PSD, is a continuous function. It is defined as the concentration of particles per unit volume and per unit increment of the particle diameter D.

Moments of the PSD can be used to characterise bulk properties of the cloud. The water content of a cloud is typically defined separately for each thermodynamic phase of water present. IWC is proportional to the third moment of the PSD and calculated, as

$$\text{IWC} = \int_0^\infty p(D)m(D)dD = \frac{\pi\rho_{ice}}{6}\int_0^\infty p(D_{veq})D_{veq}^3 dD_{veq}. \tag{3.28}$$

Note that other particle size parametrisation exist, but the above expression is only valid if the particle diameter D is taken as D_{veq}. One can also define the mean volume-weighted diameter of the cloud ice particles using the ratio of the fourth and third moments of the PSD:

$$D_{\text{m}} = \frac{\int_0^\infty p(D)D^4 dD}{\int_0^\infty p(D)D^3 dD} \tag{3.29}$$

In this chapter, atmospheric ice is often referred to interchangeably as cloud ice particles. However, frozen precipitation is also a form of atmospheric ice. Depending on the context, the variables IWC and its column integral, IWP, may refer exclusively to cloud ice or may encompass both cloud ice and frozen precipitation. In the following chapters, IWC and IWP are used to refer to *all* ice, i.e. in-cloud and precipitating.

4 The inverse problem

4.1 Solving the inverse problem

Remote observations are useful, but extracting the desired information can be challenging since the measurements are indirect. The theoretical foundation of this chapter follows Rodgers (2000), which describes how an atmospheric remote sensing observation acts a complicated function of the parameter we wish to know. This function maps the state vector $\mathbf{x}$ to the observation vector $\mathbf{y}$ as follows:

$$\mathbf{y} = f(\mathbf{x}). \tag{4.1}$$

The exact measurement $\mathbf{y}$ is generally unknown. Instead, we have a measurement accompanied by an error ϵ in the form of random noise. Since the noise cannot be known exactly and thus cannot be removed, it is instead described statistically. Furthermore, the function $f(\mathbf{x})$ is difficult to define. Although it may be possible to model $f(\mathbf{x})$ from first principles, to do so requires a thorough understanding of our observation. This includes how the sensor operates and the physics affecting the observation. Since the physics is typically complex, approximations are usually necessary. Moreover, a computational model is generally used to model the system, leading to a discretisation of the function. As a result of these factors, the *forward model* $F(\mathbf{x})$ replaces the true function:

$$\mathbf{y} = F(\mathbf{x}) + \epsilon. \tag{4.2}$$

The state $\mathbf{x}$ is the quantity of interest. This leads to the *inverse problem* — determining the state $\mathbf{x}$ of the physical system that produced the observation $\mathbf{y}$. Solving the inverse problem is inherently complex. The first consideration is whether our measurement contains sufficient information. This depends on the sensitivity of our sensor to $\mathbf{x}$.

A major challenge in solving the inverse problem is that, for atmospheric states, the problem is nonlinear. Additionally, although the forward model itself is deterministic, the inverse problem is ill-posed due to noise. In the presence of noise, the state vector $\mathbf{x}$ instead maps onto a region in the measurement space $\mathbf{y}$. Likewise, when solving the inverse problem, $\mathbf{y}$ maps onto a region of $\mathbf{x}$. Therefore, it is generally not possible to determine the exact solution for $\mathbf{x}$. In this case, it is more realistic to take a probabilistic approach, describing

this region with a probability density function (PDF).

A Bayesian approach is a useful solution to the above problem. Bayes' theorem relates the PDF of the measurement to the PDF of the state vector, taking into account any prior knowledge:

$$p(\mathbf{x}|\mathbf{y}) = \frac{p(\mathbf{y}|\mathbf{x})p(\mathbf{x})}{p(\mathbf{y})}. \tag{4.3}$$

$p(\mathbf{x})$ is the prior distribution and provides any prior knowledge of the state. The prior knowledge is then updated with measurement information $p(\mathbf{y}|\mathbf{x})$, including the noise description. $p(\mathbf{y})$ is a normalisation factor equivalent to $\int p(\mathbf{x}'|\mathbf{y})d\mathbf{x}'$. Incorporating prior knowledge about the state therefore allows the state space to be further constrained. The resulting distribution $p(\mathbf{x}|\mathbf{y})$, i.e. the posterior distribution, represents all the knowledge that we possess, thus providing better insight into the retrieved estimate.

There are multiple retrieval methods that operate within a Bayesian framework. One of the most commonly used methods is the Optimal Estimation Method (OEM, Rodgers, 2000). OEM is powerful since it allows one to obtain the Jacobian. The Jacobian provides insight into the sensitivity of the retrieval to the true state, and also enables calculation of the resolution of retrieved atmospheric profiles. However, this could also be considered a drawback, since calculating the Jacobian is computationally costly. Another disadvantage of OEM is that it assumes Gaussian statistics for both the posterior distribution and the measurement noise. Although this approach automatically provides uncertainty estimates and error correlations within the Gaussian covariance matrix, assuming a Gaussian is fairly unrealistic in most cases.

A posterior distribution that is not constrained to be a Gaussian is often preferable. Methods such as Markov Chain Monte Carlo (MCMC) may be used to compute a non-Gaussian posterior distribution for each retrieval case. Unfortunately, MCMC is computationally expensive since it requires the forward model to be repeatedly evaluated. Due to this impracticality, MCMC is generally seen as more useful for validating other retrieval models and their uncertainty estimates (Evans et al., 2012; Tamminen and Kyrölä, 2001).

Bayesian Monte Carlo Integration (BMCI) is also an effective method to retrieve posterior distributions. The requirement for BMCI is a precalculated database of forward model simulations. Although computationally expensive to initially produce, no further simulations are required for the retrievals themselves. However, one drawback to BMCI is that, although a Gaussian posterior distribution is not assumed, the method still assumes Gaussian measurement errors. BMCI has been used successfully for remote sensing retrievals, for example in Evans et al. (2002) and, notably, plans for operational ICI retrievals at EUMETSAT (Eriksson et al., 2020).

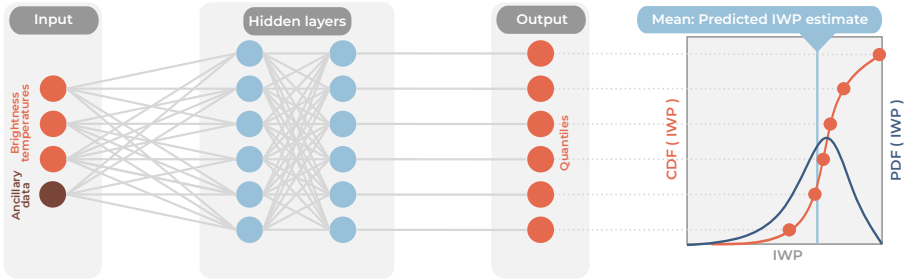

Figure 4.1: An example of a simple quantile regression neural network (QRNN), predicting IWP from a single observation. The network takes an input observation in the form of brightness temperatures across multiple frequencies, plus ancillary data, e.g. surface type. The inputs are passed through a series of hidden layers. In this example, the final layer is specific to each output variable. The output variables are quantiles of a CDF of IWP. One can interpolate between the predicted quantiles to obtain a continuous CDF, which can then be transformed into a PDF. Finally, if desired, the mean of the CDF can serve as a single estimate of IWP.

An increasingly popular alternative to the traditional Bayesian methods is machine learning. Generally, machine learning requires no assumption on the distributions of the noise or the target variables. Additionally, it allows for the easy inclusion of ancillary data. Overall, machine learning has two major advantages — it is flexible and fast.

4.2 Machine learning as a retrieval approach

Machine learning requires the existence of training data, which serves as the basis for teaching the model how to map an input $\mathbf{x}$ to an output $\mathbf{y}$. It is important to note that, in the context of machine learning, the terminology used in Section 4.1 is now reversed, i.e. the input to the model $\mathbf{x}$ represents the observation and the model target, or output, $\mathbf{y}$ is the atmospheric state.

One benefit of machine learning is its flexibility; a range of data can be included in the input, including different sensors and auxiliary data. However, most machine learning techniques are trained to predict a single estimate for a given input. As discussed in Section 4.1, the retrieval of an error estimate or a posterior distribution is preferable for atmospheric observations.

An alternative is to consider the retrieval of a discrete cumulative distribution function (CDF). This can be achieved through the use of a Quantile Regression Neural Network (QRNN), as described by Pfreundschuh et al. (2018), who provided the foundations for applying QRNN methods to atmospheric remote sensing retrievals. The CDF is defined as the integral of the posterior

distribution:

$$F_{(\mathbf{x}|\mathbf{y})} = \int_{-\infty}^{x} p(\mathbf{x}'|\mathbf{y}) d\mathbf{x}'. \tag{4.4}$$

The τth quantile x_τ of the CDF is defined as

$$x_\tau = \inf\{x : F(x) \geq \tau\}, \tag{4.5}$$

where $\tau \in [0, 1]$. Instead of minimising a loss function that targets a single estimate, such as the mean or the median, as a conventional neural network may do, QRNN uses a quantile loss function. The quantile loss function is defined as

$$\mathcal{L}_\tau(x_\tau, x) = \begin{cases} \tau|x - x_\tau|, & x_\tau < x \\ (1-\tau)|x_\tau - x|, & \text{otherwise.} \end{cases} \tag{4.6}$$

The aim is to calculate the loss between the predicted and the target values for a quantile x_τ, and to minimise the expectation of the loss.

The specific quantiles can be pre-specified and predicted independently. This allows a discrete approximation of the continuous CDF to be obtained. From the CDF, a PDF can be easily computed. The PDF can be considered to be a posterior distribution if we consider the knowledge contained within the training data to be a priori knowledge. An illustration of a simplified QRNN and a final retrieved PDF and CDF is shown in Fig. 4.1.

5 The Ice Cloud Imager

5.1 Instrument details

The Ice Cloud Imager (ICI) will be hosted as part of the EUMETSAT Polar System - Second Generation (EPS-SG) mission. EPS-SG consists of two satellites: MetOp-SG A and MetOp-SG B. MetOp-SG A will host sounding instruments, including visible, infrared, and microwave sensors (EUMETSAT, 2022). MetOp-SG B will instead host imaging sensors, such as ICI (Mattioli et al., 2019). The primary objective of the MetOp-SG satellites is to provide observations in support of NWP and climate monitoring. At the time of writing, the expected launch date of the Metop-SG B satellite is August 2026 (Fadrique, 2024).

There will be three successive launches of the pair of satellites. Since the nominal lifetime of each satellite is ∼7.5 years, ICI will provide continuous coverage for approximately 22 years. The Metop-SG satellites will fly at an altitude between 823 and 843 km, and will have a sun-synchronous orbit.

The ICI instrument is a conically scanning radiometer that will observe at an incidence angle of 53±2°. The observation swath width will be ∼1700 km, enabling ICI to provide global coverage on a daily basis. Further details on the instrument are provided in Bergadá et al. (2016) and Eriksson et al. (2020).

The thirteen channels of ICI span a frequency range from 183 GHz to 664 GHz. The channels can be divided into two groups:

- *Water vapour transition channels.*
  Three groups of channels cover the water vapour transition lines, and are centred around:
  - 183.31 GHz.
  - 325.15 GHz.
  - 448.0 GHz.

  Each of these three groups contains three individual channels, totalling nine channels. These channels measure at vertical polarisation.
- *Window channels.*
  These channels are named as such since less absorption by atmospheric

gases occurs at these frequencies, allowing for increased penetration into the atmosphere relative to the other channels.

- 243.2 GHz.
- 664.0 GHz.

At each of the above frequencies, there is a channel measuring at vertical polarisation and a channel measuring at horizontal polarisation, totalling four channels. The inclusion of multiple polarisations allows observations to capture the effects of oriented ice particles and polarisation arising from surface interactions.

Alongside ICI, the Microwave Imager (MWI) will be hosted on the MetOp-SG B satellite (Lupi et al., 2016). Similarly to ICI, MWI is a conically scanning radiometer that will observe at a 53° incidence angle. ICI and MWI are designed to compliment each other in their frequency range; MWI will measure at frequencies between 18.7 GHz and 183 GHz, extending the total frequency coverage of the pair of sensors down to lower frequencies. This is motivated by the fact that MWI will have higher sensitivity to snow and rain, whereas ICI will be primarily sensitivity to cloud ice. Together, the two sensors achieve an impressive and unmatched frequency coverage, allowing for observations of both frozen and solid water.

5.2 ICI data

The ICI measurements offered in the level-1b product at EUMETSAT will take the form of calibrated and geolocated brightness temperatures. Cloud ice variables will be provided in the level-2 (L2) product, MWI-ICI-L2, offered by EUMETSAT. MWI-ICI-L2 is based on both MWI and ICI observations. The primary variables in MWI-ICI-L2 will be liquid water path (LWP) and IWP. However, retrievals for each of these variables will be performed separately, based on the sensor used.

ICI data will be used for retrievals of IWP. As part of the ICI-specific retrievals, the L2 product will also offer the variables mean mass height (Z_{m}) and mean mass diameter (D_{m}). All variables offered in the ICI level-2 product are *column integrated* variables; they cover the entire atmospheric column, and do not contain information on the vertical variability.

To retrieve the L2 products from ICI level-1b data, EUMETSAT will perform a series of pre-processing steps. This includes the remapping of the level-1b data to the same footprint, as presented in Eriksson et al. (2020). Additionally, bias correction will be applied if any systematic differences arise between real observations and simulated cases. The full algorithm theoretical basis document (ATBD) is provided by Rydberg (2018). After the pre-processing steps, EUMETSAT will implement BMCI to perform the inversion.

The main objective of ICI is to provide the aforementioned geophysical quantities in support of climate applications. One use is to constrain global climate models, as motivated in Section 1. Information on D_{m} will be particularly useful, due to the high sensitivity of ICI to particle size, which benefits climate model representation of particle fall velocity (Buehler et al., 2007).

Another use of the data is climate monitoring. As a result of the relatively long lifetime of ICI, there will eventually exist an approximately 22 year record of atmospheric ice mass. A long-term reliable data source may prove to be valuable either for climate model validation, or for simply improving our understanding of how the distribution and amount of ice clouds is developing over time.

Although it is not the main purpose of ICI, level-1b data can be beneficial to NWP in several ways. Cloudy ICI observations can provide a wealth of information on ice particle properties, such as particle effective radius, that can benefit weather models (Geer et al., 2017). These cloudy observations will therefore be most useful when included in all-sky assimilation (Geer et al., 2018). However, even clear-sky NWP assimilation methods could benefit from cloudy observations, despite not assimilating them directly. For example, sub-millimetre observations have been shown to improve the identification of cloudy cases (Kaur et al., 2021), enabling such cases to be accurately filtered out. Furthermore, the higher frequency channels of ICI still provide additional information on water vapour.

The potential of ICI to provide cloud ice information is not limited to the official EUMETSAT L2 product. Contained within ICI radiances is likely information on additional variables. Observations are influenced by a multitude of factors including, but not limited to, the characteristics of ice hydrometeors and the distribution of ice within the atmospheric column. In fact, ICI channels undergo varying degrees of attenuation dependent on altitude. This means that brightness temperatures measured by different channels are sensitive to ice in different atmospheric layers. By virtue of the range of frequencies covered by ICI, the observations may contain information on the vertical distribution of ice. This raises the question: What more can we learn from the novel data to be provided by ICI?

6 Summary of appended papers and outlook

6.1 Paper 1

Solving the inverse problem requires information on the observations and the atmospheric state that led to the observation. In the context of ICI, this takes the form of a retrieval database consisting of pairs of ICI observations and the geophysical quantities of interest, e.g. IWP. A retrieval database is required both in preparation for the ICI L2 product, where BMCI will be used as an inversion model, and in preparation for research-oriented retrievals, where QRNN will be used.

This raises the issue of how to create such a database in the absence of real sub-millimetre observations. An empirically-based database is evidently not possible, necessitating the simulation of ICI observations using radiative transfer calculations.

The quality of the retrievals will be highly dependent on the quality of the simulations. The radiative transfer calculations must be detailed and accurate, and any ancillary data used in the simulation inputs must be of a high standard. However, the database must also be of sufficient size to successfully train the inversion model. Therefore, these important factors must be carefully balanced with the need for computational efficiency in order to generate a high number of simulations. Finally, for the inversion to perform well under all atmospheric conditions, all variability must be captured within the database. This means that the database must be global, represent all meteorological conditions, and checked to statistically represent reality.

This study presents a framework designed to generate high-quality simulations of ICI, and was developed as part of a EUMETSAT study. The simulation framework was based upon a preliminary database previously developed (Eriksson et al., 2020), but several major changes were made to improve the quality of the simulations. This includes the consideration of oriented particles, allowing polarised channels to be simulated, and the inclusion of the full antenna pattern. The appended paper presents a detailed overview of the simulations.

Additionally, retrievals are performed using a QRNN, where inversions are performed on a subset of the data that was excluded from the QRNN training. These retrievals allow us to characterise the expected retrieval performance of ICI and to investigate the sensitivity of the retrieval performance under various conditions. Furthermore, they serve as preparation for performing retrievals with real observations once ICI is launched.

Naturally, it is not possible to validate simulated ICI observations with real ICI data prior to launch. Instead, the approach was to perform simulations of existing sensors with similarities to ICI. Four GMI channels were simulated: two channels at 166 GHz, due to these channels measuring at V- and H-polarisation, and two channels at 183 GHz. Additionally, two airborne instruments were simulated: the Microwave Airborne Radiometer Scanning System (MARSS), and ISMAR. MARSS and ISMAR serve as demonstrators for ICI, and thus allow for the validation of sub-millimetre wavelength simulations.

Simulations of GMI, ISMAR and MARSS largely agreed statistically with observations. This allowed us to conclude that the simulation framework produces accurate results. Furthermore, the simulations covered the variability of the observations, which is required for the retrieval model to be able to predict all possible atmospheric configurations. Therefore, despite the impossibility of validating ICI observations directly, the validation of the above simulations demonstrates that the framework successfully simulates polarised microwave and sub-millimetre measurements.

To explore the information content of ICI observations, the degrees of freedom (DoF) were calculated as a function of IWP and total column water vapour (WV). The degrees of freedom ranged between 3 and 10 across the range of IWP and WV considered, with the highest degree of freedom found in the region of highest IWP and highest WV. However, even down to 10^{-4} $\mathrm{kg\,m^{-2}}$, ICI measurements were shown to still have a DoF of 6 in very dry conditions.

When characterising the retrievals, ICI was found to have a sensitivity to IWP over the range of 10^{-2} $\mathrm{kg\,m^{-2}}$ to 10^{1} $\mathrm{kg\,m^{-2}}$. Retrieval performance was found to vary according to climatic conditions. Retrievals of IWP performed best at tropical latitudes. Performance decreased with increasing latitude, which is partially attributed to lower cloud top height. Retrievals also performed poorer over snow surfaces, attributed to uncertainties about the emissivity of such surfaces. However, there will be interplay between the performance under various latitudes and surface types due to the frequency of snow and sea ice increasing with higher latitudes.

As a result of the simulation database generated in this study, L2 retrievals will be available at EUMETSAT from the first day of ICI's operational phase. Furthermore, the database provides the base for a research L2 product, presented in Section 6.2.

6.2 Paper 2

Information on the vertical distribution of cloud ice is highly valuable to climate applications. Unfortunately, there are very few datasets that currently offer reliable estimates. This improves with the recent launch of EarthCARE. However, non-radar/lidar sensors generally do not provide useful data due to their limited sensitivity to the entire atmospheric column, although CCIC has shown that it is possible with machine learning. However, the 13 channels of ICI undergo varying amounts of attenuation, thus providing information at different altitudes. Motivated by the need for additional datasets, this study asks: can ICI provide data on cloud ice profiles?

Radar is considered the gold standard for IWC retrievals. The signal can penetrate the entire cloud column and provide data at a high vertical resolution. It cannot be expected that a passive microwave instrument would achieve similarly high quality retrievals at a comparable resolution. However, ICI does have several advantages. Firstly, the expected combined lifetime of ICI (∼21 years) is longer than EarthCARE (∼3 years). Secondly, the ICI swath is much wider than that of a radar, allowing a retrieval to include horizontal information. Therefore, ICI and EarthCare are not competitors, but rather ICI offers a complimentary source of data.

In this study, the retrieval database developed in Paper 1 is used to train a QRNN to predict IWC and vertical profiles of mean mass diameter $D_{\mathrm{m,IWC}}$. The profiles are retrieved at a 500 m resolution.

A qualitative comparison of retrieved and reference profiles, i.e. the corresponding database cases, reveals that ICI is able to successfully retrieve both the structure and magnitude of IWC and $D_{\mathrm{m,IWC}}$. The retrievals are somewhat limited due to performing the profile inversions case-by-case, and thus neglecting correlations between profiles. This leads to some instability between neighbouring profiles, caused by statistical fluctuations between retrievals. Retrieval performance is investigated for individual altitudes. Performance is best at mid-altitudes, with sensitivity to IWC ranging between 10^{-2} g m^{-3} and 1 g m^{-3}. At the highest and lowest altitudes, the retrieval performance worsens due to the decreased sensitivity of ICI in these regions. A statistical comparison to IWC in the DARDAR product shows good agreement.

Since the true resolution of ICI retrievals is expected to be less than 500 m, the question is asked: What is the expected resolution of our retrievals? To investigate further, an approximation of the averaging kernels is computed on a near-linear subset of the IWC and $D_{\mathrm{m,IWC}}$ retrievals, following the method in Rydberg et al. (2009). At mid-altitudes, it is shown that ICI can be expected to retrieve IWC at a resolution of ∼2.5 km. In the case of $D_{\mathrm{m,IWC}}$ profile retrievals, the expected resolution tends to increase with altitude, with a minimum of 2.5 km resolution at an altitude of 5 km.

The conclusion of the study is that ICI observations do contain sufficient information to retrieve vertical profiles of atmospheric ice. Some instability arises due to retrieving profiles individually, although this could be approached in further research by accounting for correlations between profiles when performing the inversions. ICI could therefore act as a complimentary data source to existing IWC datasets. Excitingly, such retrievals will be the first of their kind; no existing dataset provides cloud ice vertical profiles from passive microwave observations.

6.3 Outlook

6.3.1 AWS

With the launch of AWS in August 2024 came the first operational measurements of the atmosphere at sub-millimetre wavelengths.

The inclusion of sub-millimetre channels on AWS was motivated by their potential to improve NWP models. The 325 GHz channels will be assimilated at ECMWF (European Centre for Medium-Range Weather Forecasts). Although sub-millimetre observations will not be assimilated in the near future at SMHI (The Swedish Meteorological and Hydrological Institute), they will instead be used for cloud filtering. Cloud filtering is the removal of the impact of clouds in assimilated observations.

One method of cloud filtering involves identifying cloudy cases using the difference between an AWS observation (i.e. all-sky) and a clear-sky observation. Simulating AWS using the same framework as used for ICI, altering for the sensor geometry and characteristics of AWS, provides a dataset of all-sky observations and matching clear-sky observations. These simulations can then be used to train a QRNN to predict a clear-sky antenna temperature when given a real AWS measurement. Kaur et al. (2021) has shown that the use of sub-millimetre channels offers a benefit to this method. If the method can be demonstrated to be successful for AWS, there are plans to incorporate the approach in SMHI NWP models.

At the time of publication, the first data is arriving from AWS. This takes the form of level-1b data, i.e. geolocated and calibrated antenna temperatures. However, there is no L2 product currently planned for AWS. Considering the ICI retrieval performance demonstrated in May et al. (2024), i.e. Paper 1, it is expected that AWS can also provide reliable estimates of IWP, Z_{m}, and D_{m}. We are currently in the early stage of developing retrievals of IWP, Z_{m}, and D_{m} from AWS observations, taking the same approach as for ICI.

Performing AWS retrievals has several added advantages. Firstly, our AWS simulations can be validated against real observations. This means that calibrations and adjustments can be made to the simulations if needed. Secondly, it

will be possible to validate the retrievals themselves through comparison with existing operational products, such as CCIC.

A comparison of simulated radiances with real radiances may also provide a better understanding of the approach and assumptions made in the simulation framework. For example, one can analyse how the chosen microphysical models affect the simulations relative to the truth. A better understanding of the impact of choices made in the simulation framework will provide a deeper insight into retrieval performance, both for AWS and for ICI.

References

Amell, A., S. Pfreundschuh and P. Eriksson (2024). 'The Chalmers Cloud Ice Climatology: retrieval implementation and validation'. In: *Atmos. Meas. Tech.* 17.14, pp. 4337–4368. DOI: 10.5194/amt-17-4337-2024 (cit. on p. 10).

Bergadá, M., M. Labriola, R. González et al. (2016). 'The Ice Cloud Imager (ICI) preliminary design and performance'. In: *2016 14th Specialist Meeting on Microwave Radiometry and Remote Sensing of the Environment (MicroRad)*, pp. 27–31. DOI: 10.1109/MICRORAD.2016.7530498 (cit. on p. 25).

Bony, S., B. Stevens, D. M. W. Frierson et al. (2015). 'Clouds, circulation and climate sensitivity'. In: *Nat. Geosci.* 8.4, pp. 261–268. DOI: 10.1038/ngeo2398 (cit. on p. 3).

Brath, M., S. Fox, P. Eriksson, R. C. Harlow, M. Burgdorf and S. A. Buehler (2018). 'Retrieval of an ice water path over the ocean from ISMAR and MARSS millimeter and submillimeter brightness temperatures'. In: *Atmos. Meas. Tech.* 11.1, pp. 611–632. DOI: 10.5194/amt-11-611-2018 (cit. on p. 11).

Buehler, S. A., C. Jiménez, K. F. Evans et al. (2007). 'A concept for a satellite mission to measure cloud ice water path, ice particle size, and cloud altitude'. In: *Q. J. R. Meteorol. Soc.* 133.S2, pp. 109–128. DOI: 10.1002/qj.143 (cit. on p. 27).

Cesana, G. V., A. S. Ackerman, T. V. de Guélis and D. S. Henderson (2023). 'Cloud-Radiation Interactions and Cloud-Climate Feedbacks From an Active-Sensor Satellite Perspective'. In: *Clouds and Their Climatic Impacts*. American Geophysical Union (AGU), pp. 87–102. ISBN: 978-1-119-70035-7. DOI: 10.1002/9781119700357.ch4 (cit. on p. 8).

Delanoë, J. and R. J. Hogan (2010). 'Combined CloudSat-CALIPSO-MODIS retrievals of the properties of ice clouds'. In: *J. Geophys. Res. Atmos.* 115.D4. DOI: 10.1029/2009JD012346 (cit. on p. 10).

Deng, M., G. G. Mace, Z. Wang and H. Okamoto (2010). 'Tropical Composition, Cloud and Climate Coupling Experiment validation for cirrus cloud profiling retrieval using CloudSat radar and CALIPSO lidar'. In: *J. Geophys. Res. Atmos.* 115.D10. DOI: 10.1029/2009JD013104 (cit. on p. 10).

Duncan, D. and P. Eriksson (2018). 'An update on global atmospheric ice estimates from satellite observations and reanalyses'. In: *Atmos. Chem. Phys.* 18.15, pp. 11205–11219. DOI: 10.5194/acp-18-11205-2018 (cit. on p. 4).

eoPortal (2024). *AWS (Arctic Weather Satellite)*. URL: https://www.eoportal.org/satellite-missions/aws (visited on 2024-11-12) (cit. on p. 11).

Eriksson, P., B. Rydberg, H. Sagawa, M. S. Johnston and Y. Kasai (2014). 'Overview and sample applications of SMILES and Odin-SMR retrievals of upper tropospheric humidity and cloud ice mass'. In: *Atmospheric Chem. Phys.* 14.23, pp. 12613–12629. DOI: 10.5194/acp-14-12613-2014 (cit. on p. 10).

Eriksson, P., M. Ekström, B. Rydberg and D. Murtagh (2007). 'First Odin sub-mm retrievals in the tropical upper troposphere: ice cloud properties'. In: *Atmospheric Chem. Phys.* 7.2, pp. 471–483. DOI: 10.5194/acp-7-471-2007 (cit. on p. 10).

Eriksson, P., B. Rydberg, V. Mattioli, A. Thoss, C. Accadia, U. Klein and S. A. Buehler (2020). 'Towards an operational Ice Cloud Imager (ICI) retrieval product'. In: *Atmos. Meas. Tech.* 13.1, pp. 53–71. DOI: 10.5194/amt-13-53-2020 (cit. on pp. 22, 25, 26, 29).

EUMETSAT (2022). *Metop - Second Generation*. URL: https://www.eumetsat.int/metop-sg (visited on 2024-11-12) (cit. on p. 25).

— (2024). *EPS Sterna*. last access: 25 October 2024, https://www.eumetsat.int/eps-sterna. URL: https://www.eumetsat.int/eps-sterna (visited on 2024-10-01) (cit. on p. 11).

Evans, K. F., J. R. Wang, D. O'C Starr, G. Heymsfield, L. Li, L. Tian, R. P. Lawson, A. J. Heymsfield and A. Bansemer (2012). 'Ice hydrometeor profile retrieval algorithm for high-frequency microwave radiometers: application to the CoSSIR instrument during TC4'. In: *Atmos. Meas. Tech.* 5.9, pp. 2277–2306. DOI: 10.5194/amt-5-2277-2012 (cit. on p. 22).

Evans, K. F., S. J. Walter, A. J. Heymsfield and G. M. McFarquhar (2002). 'Submillimeter-wave cloud ice radiometer: simulations of retrieval algorithm performance'. In: *J. Geophys. Res. Atmos.* 107.D3, AAC 2–1–AAC 2–21. DOI: 10.1029/2001JD000709 (cit. on p. 22).

Fadrique, F. M. (2024). *EPS-SG Programme Overview and Status*. Conference presentation. Würzburg, Germany: EUMETSAT Meteorological Satellite Conference 2024 (cit. on p. 25).

Geer, A. J., F. Baordo, N. Bormann, P. Chambon, S. J. English, M. Kazumori, H. Lawrence, P. Lean, K. Lonitz and C. Lupu (2017). 'The growing impact of satellite observations sensitive to humidity, cloud and precipitation'. In: *Q. J. Roy. Meteor. Soc.* 143.709, pp. 3189–3206. DOI: 10.1002/qj.3172 (cit. on p. 27).

Geer, A. J., K. Lonitz, P. Weston et al. (2018). 'All-sky satellite data assimilation at operational weather forecasting centres'. In: *Q. J. R. Meteorol. Soc.* 144.713, pp. 1191–1217. DOI: 10.1002/qj.3202 (cit. on p. 27).

Heymsfield, A. J., A. Protat, D. Bouniol et al. (2008). 'Testing IWC retrieval methods using radar and ancillary measurements with in situ data'. In: *J. Appl. Meteorol. Clim.* 47.1, pp. 135–163. DOI: 10.1175/2007JAMC1606.1 (cit. on p. 10).

Illingworth, A. J., H. W. Barker, A. Beljaars et al. (2015). 'The EarthCARE satellite: the next step forward in global measurements of clouds, aerosols,

precipitation, and radiation'. In: *Bull. Am. Meteorol. Soc.* 96.8, pp. 1311–1332. DOI: 10.1175/BAMS-D-12-00227.1 (cit. on p. 10).

IPCC (2021). *Climate Change 2021: The Physical Science Basis. Contribution of Working Group I to the Sixth Assessment Report of the Intergovernmental Panel on Climate Change*. Ed. by V. Masson-Delmotte, P. Zhai, A. Pirani et al. Cambridge University Press (cit. on pp. 3, 4).

Kaur, I., P. Eriksson, S. Pfreundschuh and D. I. Duncan (2021). 'Can machine learning correct microwave humidity radiances for the influence of clouds?' In: *Atmos. Meas. Tech.* 14.4, pp. 2957–2979. DOI: 10.5194/amt-14-2957-2021 (cit. on pp. 27, 32).

Kummerow, C. D., D. L. Randel, M. Kulie, N.-Y. Wang, R. Ferraro, S. J. Munchak and V. Petkovic (2015). 'The evolution of the goddard profiling algorithm to a fully parametric scheme'. In: *J. Atmos. Ocean. Tech.* 32.12, pp. 2265–2280. DOI: 10.1175/JTECH-D-15-0039.1 (cit. on p. 10).

Lupi, T., F. Tominetti, M. Grilli et al. (2016). 'Microwave imager instrument for MetOp second generation: Design and verification'. In: *2016 14th Specialist Meeting on Microwave Radiometry and Remote Sensing of the Environment (MicroRad)*, pp. 32–36. DOI: 10.1109/MICRORAD.2016.7530499 (cit. on p. 26).

Mattioli, V., C. Accadia, J. Ackermann, S. Di Michele, I. Hans, P. Schlüssel, P. Colucci and A. Canestri (2019). 'The EUMETSAT Polar System - Second Generation (EPS-SG) Passive Microwave and Sub-mm Wave Missions'. In: *PhotonIcs & Electromagnetics Research Symposium*, pp. 3926–3933. DOI: 10.1109/PIERS-Spring46901.2019.9017822. (Visited on 2024-03-06) (cit. on p. 25).

Matus, A. V. and T. S. L'Ecuyer (2017). 'The role of cloud phase in Earth's radiation budget'. In: *J. Geophys. Res. Atmos.* 122.5, pp. 2559–2578. DOI: 10.1002/2016JD025951 (cit. on p. 3).

May, E., B. Rydberg, I. Kaur, V. Mattioli, H. Hallborn and P. Eriksson (2024). 'The Ice Cloud Imager: retrieval of frozen water column properties'. In: *Atmos. Meas. Tech.* 17.19, pp. 5957–5987. DOI: 10.5194/amt-17-5957-2024 (cit. on p. 32).

Millán, L., W. Read, Y. Kasai, A. Lambert, N. Livesey, J. Mendrok, H. Sagawa, T. Sano, M. Shiotani and D. L. Wu (2013). 'SMILES ice cloud products'. In: *J. Geophys. Res. Atmos.* 118.12, pp. 6468–6477. DOI: 10.1002/jgrd.50322 (cit. on p. 10).

Mülmenstädt, J., O. Sourdeval, J. Delanoë and J. Quaas (2015). 'Frequency of occurrence of rain from liquid-, mixed-, and ice-phase clouds derived from A-Train satellite retrievals'. In: *Geophys. Res. Lett.* 42.15, pp. 6502–6509. DOI: 10.1002/2015GL064604 (cit. on p. 3).

Pfreundschuh, S., P. Eriksson, D. Duncan, B. Rydberg, N. Håkansson and A. Thoss (2018). 'A neural network approach to estimating a posteriori distributions of Bayesian retrieval problems'. In: *Atmos. Meas. Tech.* 11.8, pp. 4627–4643. DOI: 10.5194/amt-11-4627-2018 (cit. on p. 23).

Pfreundschuh, S., S. Fox, P. Eriksson, D. Duncan, S. A. Buehler, M. Brath, R. Cotton and F. Ewald (2022). 'Synergistic radar and sub-millimeter radiometer retrievals of ice hydrometeors in mid-latitude frontal cloud

systems'. In: *Atmos. Meas. Tech.* 15.3, pp. 677–699. DOI: 10.5194/amt-15-677-2022 (cit. on p. 11).

Platnick, S., M. King, S. Ackerman, W. Menzel, B. Baum, J. Riedi and R. Frey (2003). 'The MODIS cloud products: algorithms and examples from terra'. In: *IEEE T. Geosci. Remote* 41.2, pp. 459–473. DOI: 10.1109/TGRS.2002.808301. (Visited on 2023-04-26) (cit. on p. 10).

Rodgers, C. D. (2000). *Inverse methods for atmospheric sounding: theory and practice*. Vol. 2. Series on Atmospheric, Oceanic and Planetary Physics. World Scientific. ISBN: 978-981-02-2740-1. DOI: 10.1142/3171 (cit. on pp. 21, 22).

Rydberg, B., P. Eriksson, S. A. Buehler and D. P. Murtagh (2009). 'Non-Gaussian Bayesian retrieval of tropical upper tropospheric cloud ice and water vapour from Odin-SMR measurements'. In: *Atmos. Meas. Tech.* 2.2, pp. 621–637. ISSN: 1867-1381. DOI: 10.5194/amt-2-621-2009 (cit. on p. 31).

Rydberg, B. (2018). 'EPS-SG ICI ice water path product: ATBD'. In: URL: https://research.chalmers.se/en/publication/514522 (visited on 2024-11-16) (cit. on p. 26).

Space - WGClimate, C. M. from (2024). *ECV Inventory*. URL: https://climatemonitoring.info/ecvinventory/ (visited on 2024-10-16) (cit. on p. 3).

Stephens, G. L. (2005). 'Cloud Feedbacks in the Climate System: A Critical Review'. In: *J. Clim.* 18.2, pp. 237–273. DOI: 10.1175/JCLI-3243.1 (cit. on p. 4).

Tamminen, J. and E. Kyrölä (2001). 'Bayesian solution for nonlinear and non-Gaussian inverse problems by Markov chain Monte Carlo method'. In: *Journal of Geophysical Research: Atmospheres* 106.D13, pp. 14377–14390. DOI: https://doi.org/10.1029/2001JD900007 (cit. on p. 22).

Waliser, D. E., J.-L. F. Li, C. P. Woods et al. (2009). 'Cloud ice: A climate model challenge with signs and expectations of progress'. In: *J. Geophys. Res. Atmos.* 114.D8. DOI: 10.1029/2008JD010015 (cit. on p. 4).

Wu, D., J. Jiang and C. Davis (2006). 'EOS MLS cloud ice measurements and cloudy-sky radiative transfer model'. In: *IEEE. Trans. Geosci. Remote. Sens.* 44.5, pp. 1156–1165. DOI: 10.1109/TGRS.2006.869994 (cit. on p. 10).